Supporting Materials for

Electrodeposited Self-assembled Monolayers for Improving the Efficiency and Stability of Perovskite Solar Cells

Zhihui Xiong†, Xuanang Luo†, Fushen Tang†, Bohan Wang, Sen Yin, Yu Li, Zhangyu Yuan, Chenxi Peng, Shaohua Tong, Jialin Wu, Xingwang Kang, Ganlin Liu, Ying Wang, Youran Lin, Mingke Li, Yulong Li, Yuanyuan Shu, Wei Meng, Ning Li*, Lei Ying*

Institute of Polymer Optoelectronic Materials and Devices, Guangdong Basic Research Center of Excellence for Energy and Information Polymer Materials, State Key Laboratory of Luminescent Materials and Devices, South China University of Technology, Guangzhou 510640, China.

†These authors contributed equally to this work.

Corresponding E-mail: N.L. ningli2022@scut.edu.cn; L.Y. msleiying@scut.edu.cn;

Supplementary Note 1: Fabrication of electrodeposited layers

Materials

Except for TBAPF6, all reagents were used as received without further purification. The (2-(9H-Carbazol-9-yl)ethyl)phosphonic acid (2PACz), N-(2-cyanoethyl)carbazole (Cz-CN), N-carbazole–adamantyl (Cz–Py) and N-(2-adamantylethyl)carbazole (Cz–Adm) were sourced from Dongguan Volt-Amp Optoelectronics Tech Co. Ltd. (China). Formamidinium iodide (FAI), lead iodide (PbI_2), cesium iodide (CsI), methylammonium bromide (MABr), methylamine hydrochloride (MACl), and piperazinium iodide (PI) were purchased from Xi'an Yuri Solar Co., Ltd. (China). N,N-dimethylformamide (DMF), dimethyl sulfoxide (DMSO), tetrabutylammonium hexafluorophosphate ($TBAPF_6$), ethanol (EtOH), acetonitrile (ACN), chlorobenzene (CB) and isopropanol (IPA) were anhydrous and purchased from J&K Scientific.

Fabrication of Spin-coated 2PACz

The spin-coated monolayer 2PACz film fabrication began by cleaning ITO glass substrates via ultrasonic treatments in acetone, detergent, deionized water, and 2-propanol, followed by drying at 80 °C. Next, the cleaned substrates underwent a 5-minute oxygen plasma treatment before being transferred into a glove box. Subsequently, a 2PACz solution (1 mg mL^{-1} in ethanol) was spin-coated onto the ITO at 3000 rpm and then thermally annealed at 100 °C for 10 minutes.

Fabrication of electrodeposited 2PACz

First, cleaning ITO glass substrates via ultrasonic treatments in acetone, detergent, deionized water, and 2-propanol, then drying them at 80 °C. A solution containing 2PACz (1 mg mL^{-1}) and tetrabutylammonium hexafluorophosphate ($TBAPF_6$, 0.1 M) in a 1:10 mixture of acetonitrile and ethanol served as the electrolyte solution. All components were placed in a glove box, where the cleaned ITO substrate was immersed in the electrolyte and connected as the working electrode in a three-electrode system. A platinum (99.99%) plate was used as the counter electrode, and a RE-7 (Ag/Ag^+) reference electrode was employed for the non-aqueous environment. A potential scan range of 0.4 to −2.15 V was applied via electrochemical workstation. During this scan, 2PACz on ITO underwent reductive reactions at the working

electrode/electrolyte interface, resulting in electrodeposited 2PACz being deposited onto the ITO working electrode.

Fabrication of electrodeposited 2PACz

Building on the previously electrodeposited 2PACz film, an electrochemical coupling approach was used to create the dual-functional DCPN layer. A solution of Cz–CN (1 mg mL^{-1}) and tetrabutylammonium hexafluorophosphate ($TBAPF_6$, 0.1 M) in acetonitrile served as the electrolyte. The electrodeposited ITO/2PACz substrate was immersed in this electrolyte and connected as the working electrode in a three-electrode configuration, with a platinum (99.99%) plate as the counter electrode and a RE-7 (Ag/Ag^+) reference electrode for non-aqueous environments. A potential sweep from 0 to 1.05 V was applied via electrochemical workstation. During this potential scan, the 2PACz film on the ITO underwent electrochemical oxidative coupling with Cz–CN in the electrolyte. As a result, an additional carbazole moiety was grown atop the existing 2PACz, forming the dimeric carbazole-coupled SAM (DCPN).

DCPy and DCPA were prepared using the same procedure, except that Cz–CN in the electrolyte solution was replaced with N-carbazole–adamantyl (Cz–Py) and N-(2-adamantylethyl)carbazole (Cz–Ad), respectively.

Supplementary Note 2: Fabrication perovskite solar cell

For the preparation of $Cs_{0.05}(FA_{0.95}MA_{0.05})_{0.95}Pb(I_{0.95}Br_{0.95})_3$, a 1.5 M perovskite precursor solution was prepared by mixing CsI, FAI, PbI2, MABr in a DMF: DMSO = 4:1 (vol/vol) solvent mixture according to the stoichiometric ratio. The solution was stirred for 12 hours, with an additional 3 mol% PbI_2 and 10 mol% MACl added to improve crystallization. Based on the previously prepared SAMs, we then used these various ITO/SAMs substrates to proceed with the subsequent steps of perovskite device fabrication. The perovskite layer was prepared by spin-coating the perovskite solution at 5000 rpm (ramping up from 1000 rpm over 5 s) for 30 s, during which 200 μL of anisole was dropped onto the spinning substrate in the final 12 s. The resulting film was then annealed at 110 °C for 30 min to form the perovskite layer. Next, a piperazine hydroiodide solution (0.3 mg mL^{-1} in 2-propanol) was spin-coated at 5000 rpm for 30 s and subsequently annealed at 100 °C for 5 min to serve as an interfacial passivation layer. A 20 nm C_{60} layer was deposited by thermal evaporation under high vacuum to function as the electron transport layer, followed by a 6 nm BCP cathode buffer. Finally, an Ag electrode (~100 nm) was evaporated through a shadow mask, yielding devices with an active area of 0.04 cm^2.

Supplementary Note 3: Characterization for electrodeposite layer and perovskite solar cell.

NMR measurements were performed using a Bruker AVANCE 400/500 spectrometer operating at 400 or 500 MHz, with tetramethyl silane (TMS) as the internal standard. UV-vis absorption spectra of the thin films, spin-cast on quartz glass, were recorded using a Shimadzu UV-3600 UV-vis-NIR spectrometer. UPS and XPS measurements were conducted on an Axis Supra+ (Kratos), with Ag as the reference. The contact angle tests for thin films were performed on an OCA50 contact angle goniometer, using DI water and diiodomethane. Surface energy was calculated with the Owens-Wendt-Rabel-Kaelble (OWRK) method. Field emission scanning electron microscope (FESEM) top surface and cross-section images of the perovskites were obtained on a SU8600 FESEM, Hitachi. Raman spectra were recorded on a Renishaw inVia Raman microscope with 50x object at room temperature. The wavelength for the measurement was 532 nm with 0.5 to 10% laser power dependent on the samples. XRD were obtained by using a PANalytical X'pert Powder. The perovskite phase transition behaviors were measured by an Ocean Optics DT-MINI-2-GS under nitrogen atmosphere at 60 °C.

Tapping-mode atomic force microscopy (AFM) images were obtained by using Bruker Multimode 8 Microscope. Conductive AFM (cAFM) were obtained by using Bruker Icon. Infrared AFM (IR-AFM) were obtained by using Anasys nanoIR3. Time-of-flight secondary ion mass spectrometry (TOF-SIMS) images were obtained by using an ION TOF ToF SIMS 5-100. Photoluminescence quantum yield (PLQY) and time-resolved photoluminescence (TRPL) were obtained by using FluoTime 300 fluorescence lifetime spectrometer.

The current density-voltage (J-V) curves of the devices were measured using a Keithley 2400 sourcemeter under 1 sun irradiation from an AM 1.5G solar simulator (SS-F5, Enlitech). External quantum efficiency (EQE) spectra were obtained using an EQE measurement system (QE-R, Enlitech), calibrated with a standard single-crystal Si photodetector before testing. TPV, TPC and impedance spectroscopy (EIS) measurements were conducted using the Platform for All-In-One Characterization of Solar Cells and OLED (PAIOS).

Supplementary Note 4: Characterization for electrochemical experiments and Cyclic voltammogram in a blank electrolyte solution.

Electrodeposition were performed on a CHI 760D electrochemical workstation and Metrohm Autolab PGSTAT302N electrochemical workstation in three-electrode system under a dry and oxygen-free argon atmosphere (in the nitrogen glove box). Acetonitrile (CH_3CN) with 0.1 M Tetrabutylammonium hexafluoro ($TBAPF_6$) as the supporting electrolyte was used as the electrolyte solution. Glassy carbon, carbon paper or Indium doped Tin Oxide coated glass slide (ITO) were used as the working electrode. In the preparation of films by electrodeposition using carbon paper or ITO as working electrodes, a titanium (99.99%) plate was used as the counter electrode. And in other electrochemical experiments, a platinum (99.99%) plate or wire plate was used as the counter electrode. RE-7 reference electrode for non-aqueous solution (Ag/Ag^+ type) was used as the reference electrode. CH_3CN containing 0.01 M silver nitrate ($AgNO_3$) and 0.1 M $TBAPF_6$ was used as an internal reference solution. EtOH or ACN was anhydrous solvents purchased from J&K Scientific. $TBAPF_6$ purchased from J&K Scientific was recrystallized with ethanol three times and dried before use. Glassy carbon, titanium and platinum electrodes were purchased from Tianjin Aida Hengsheng Technology Development Co., Ltd. Carbon paper was purchased from Thermo Fisher Scientific. ITO was purchased from Guangzhou New Vision Optoelectronic Technology Co. Ltd. RE-7 reference electrode for non-aqueous solution (Ag/Ag^+ type) was purchased from ALS Co., Ltd. AgNO3 (99.999%) was purchased from Sigma-Aldrich Chemistry. Before each electrochemical experiment, ferrocene (Fc) was used to calibrate the reference electrode. All potentials (if not stated otherwise) were relative to the Fc/Fc^+. Fc was purchased from J&K Scientific.

The ITO substrates coated with either spin-coated or electrodeposited 2PACz were immersed as the working electrode into a blank electrolyte solution containing $TBAPF_6$ (0.1 M in a 1:10 ethanol/acetonitrile mixture). Cyclic voltammetry was performed within a defined potential range 0 to 1.05V, during which changes in the carbazole peak current at 0.8 V were monitored. A progressive decrease in peak current intensity over consecutive scans indicates a gradual reduction in carbazole concentration at the electrolyte/electrode interface, suggesting partial desorption of 2PACz molecules from the electrode surface into the electrolyte.

Supplementary Note 5: Stability testing.

For stability assessment, inverted perovskite solar cells (PSCs) with the architecture of ITO/HTM/perovskite/C_{60}/BCP/Ag were fabricated. Operational stability tests were performed under continuous maximum power point tracking (MPPT) at 65 °C, employing a 1-sun-equivalent white-light LED illumination in N_2 air. The intensity of illumination was calibrated according to the J–V-derived current density. For the damp-heat stability evaluation, the devices were encapsulated using a UV-curable adhesive and subsequently aged in an environmental chamber maintained at 85 °C and 50% relative humidity (RH). Average device characteristics with standard deviation were obtained based on 5 cells for each set.

Supplementary Note 6: Space charge limited current (SCLC) measurement.

Hole-only devices to evaluate the trap density for perovskites deposited on various hole transport layer were fabricated with ITO/HTLs/perovskite/PTAA/Ag. The defect density Nt can be obtained by equation: $Nt = 2\varepsilon_0\varepsilon VTFL/qL^2$, where ε and ε_0 are the relative dielectric constant and vacuum permittivity. VTFL is the onset voltage of TFL region, and q and L are elementary charge and the thickness of perovskite layer, respectively.

Supplementary Note 7: Simulation.

The molecular structures for various SAMs were optimized by density functional theory (DFT) through Gaussian package, using the B3LYP-D3/6-31G** method and the IRI interaction is furtherly evaluated using Multiwfn and VMD on the basis of B3LYP-D3/deftzvp. The electron density difference (EDD) was obtained from DFT-optimized HTMs and calculated using GGA/PBE via CASTEP[59,60].

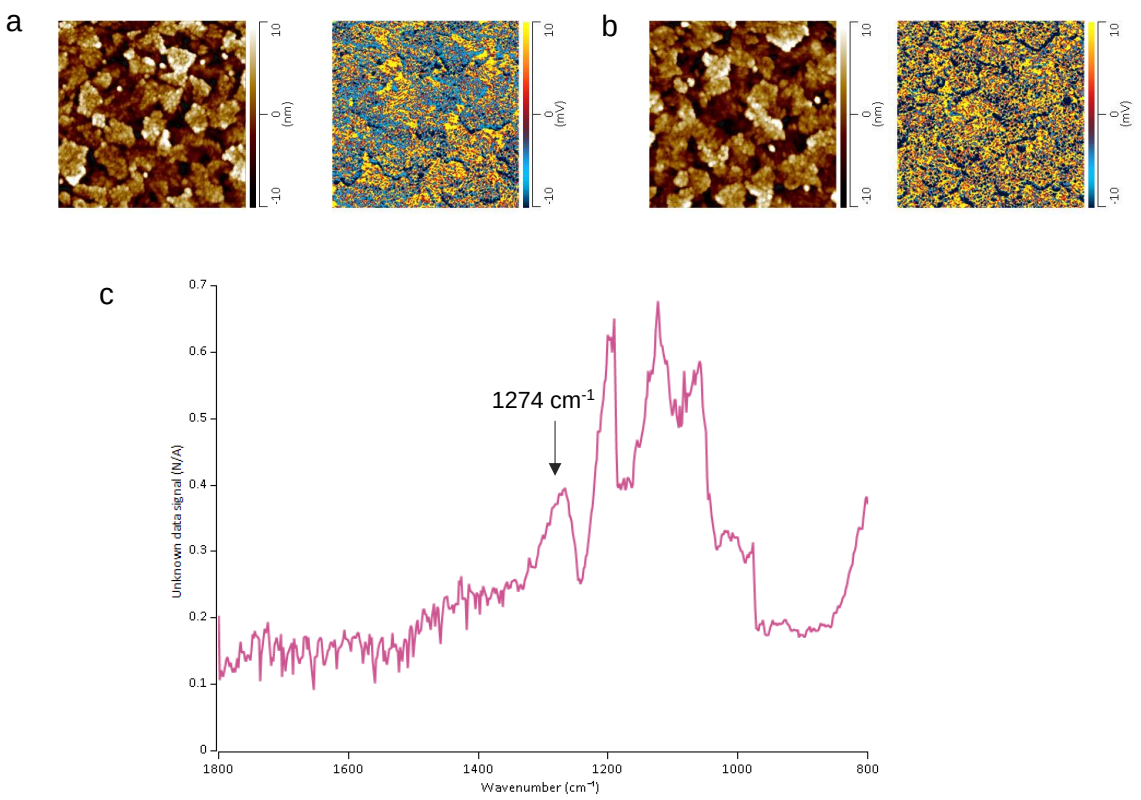

Supplementary Fig. 1. AFM and infrared AFM images of different ITO/SAM substrates: (a) Spin-coated 2PACz and (b) electrodeposited 2PACz (c) the IR-AFM spectra confirm the successful formation of the 2PACz monolayer, characterized by distinct vibrational peaks attributed to 1274 cm^{-1}.

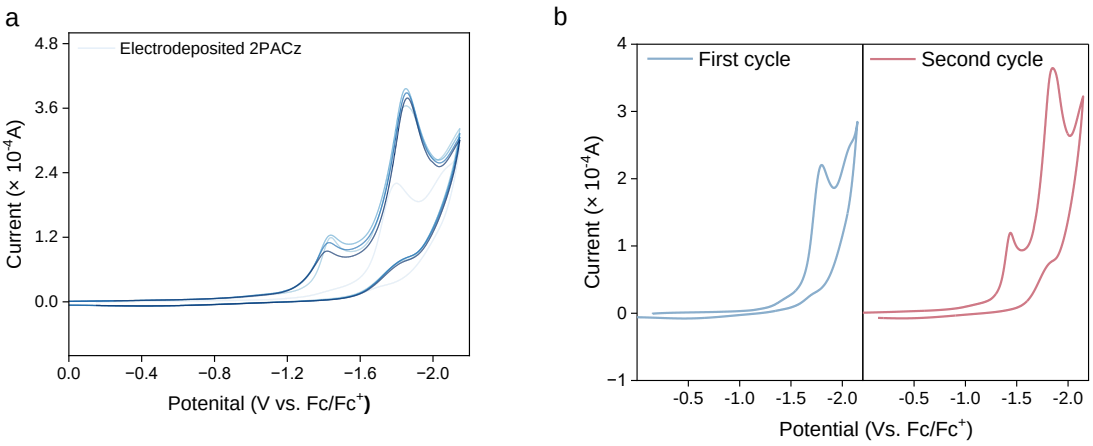

Supplementary Fig. 2. Cyclic voltammograms of electrodeposited 2PACz formation. (**a**) Cyclic voltammetry curves from the 1st to 5th cycles, with lighter curves representing earlier cycles and darker curves indicating later scans. (**b**) Comparison between the first and second scans; the emergence of a new peak at approximately −1.45 V in the second scan suggests the occurrence of a new electrochemical reaction between 2PACz and the ITO substrate during the initial potential cycle.

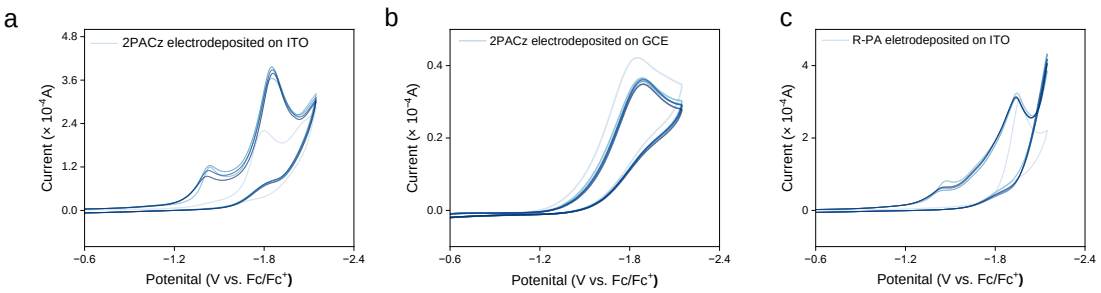

Supplementary Fig. 3. Identification of the reactive sites for electrochemical deposition via comparative cyclic voltammetry (CV). (a) Electrodeposition of 2PACz onto ITO. (b) electrodeposition of 2PACz onto a glassy carbon electrode (GCE) electrode. (c) electrodeposition of 1-butanephosphonic acid (BuPA) onto ITO. Notably, the new CV peak emerged only in the presence of both the $–PO_3H_2$ group and ITO substrate, confirming that the electrochemical reaction specifically occurs between the $–PO_3H_2$ moiety and the ITO substrate.

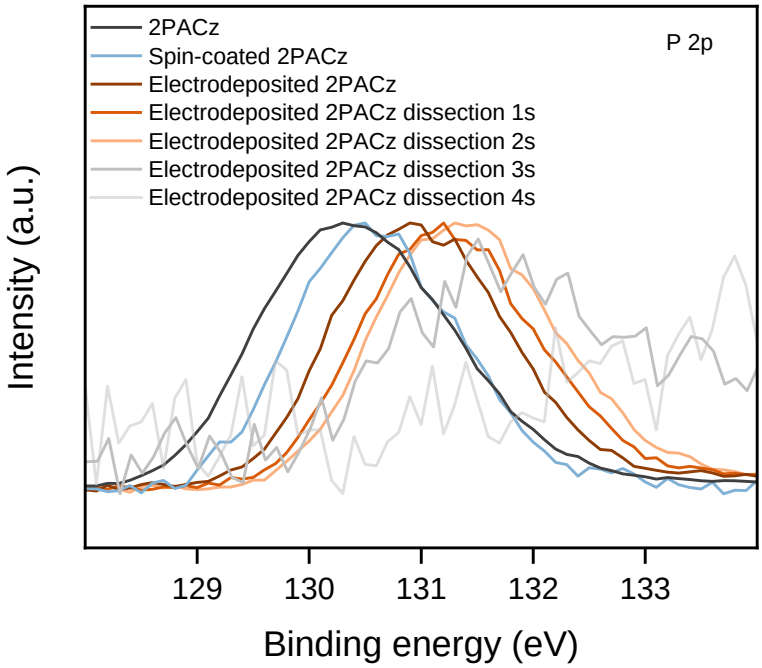

Supplementary Fig. 4.XPS analysis of P 2p signals for SAMs prepared by different methods. The electrodeposited 2PACz was analyzed using depth-dependent XPS measurements by varying the etching duration. For the pristine 2PACz monolayer (without ITO), the phosphorus signal corresponds predominantly to the P–O–H bond within the phosphonic acid group. Upon deposition onto ITO, spin-coated 2PACz exhibited a slightly increased phosphorus binding energy, indicative of interaction between phosphonic acid groups and the ITO substrate. Further, by precisely controlling the etching time in depth-profiling XPS of electrodeposited 2PACz, the bottommost interface at 2 s etching was selected as representative of direct anchoring between phosphonic acid groups and ITO, thus identifying the characteristic phosphorus signal corresponding to the P–O–In bond. This signal, reflecting the direct interaction between phosphonic acid groups and the ITO surface, serves as a reliable indicator for evaluating the anchoring strength at the SAM–ITO interface.

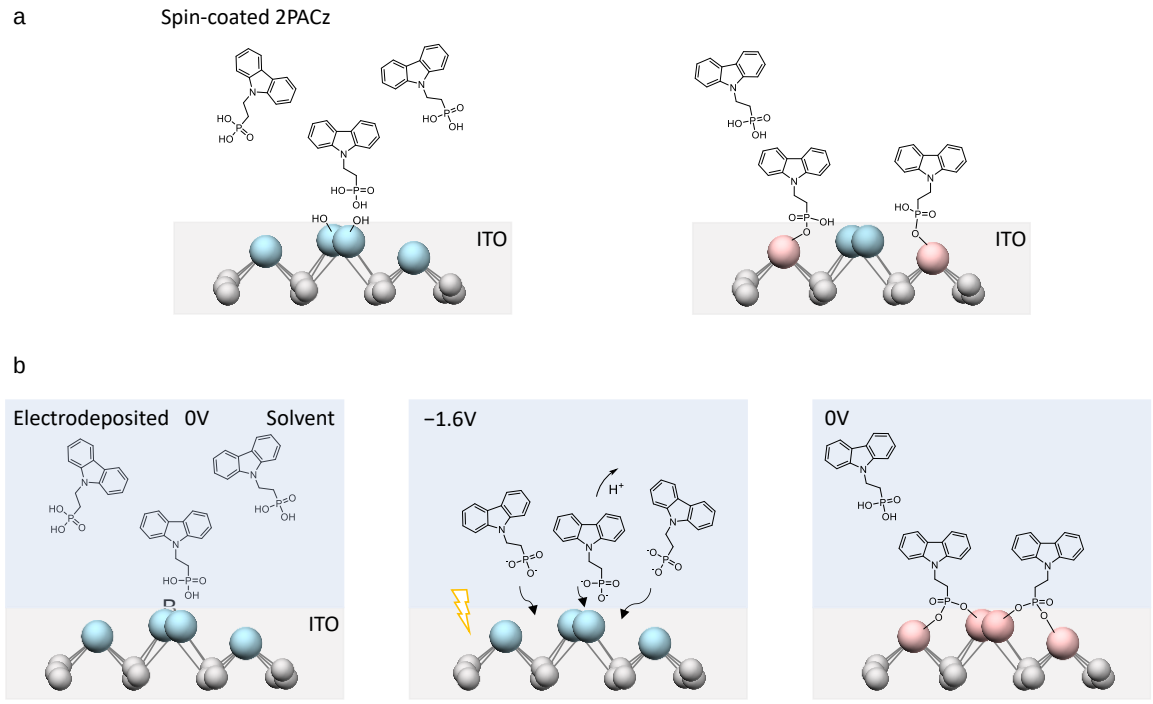

Supplementary Fig. 5. Schematic illustration comparing the anchoring mechanisms between phosphonic acid groups and the ITO substrate under spin-coating and electrodeposition methods. (a) Spin-coated 2PACz relies on surface hydroxyl (-OH) groups present on the ITO substrate, typically requiring oxygen plasma pretreatment to increase the density of surface -OH groups. Subsequently, these surface -OH groups react with the phosphonic acid groups, facilitating anchoring. (b) electrodeposited 2PACz anchoring occurs independently of surface hydroxyl groups, eliminating the need for plasma pretreatment. Under applied electrochemical potentials, 2PACz undergoes a reductive process, enabling the resulting negatively charged oxygen species to directly bind with In or Sn atoms on the ITO surface, thereby achieving robust anchoring.

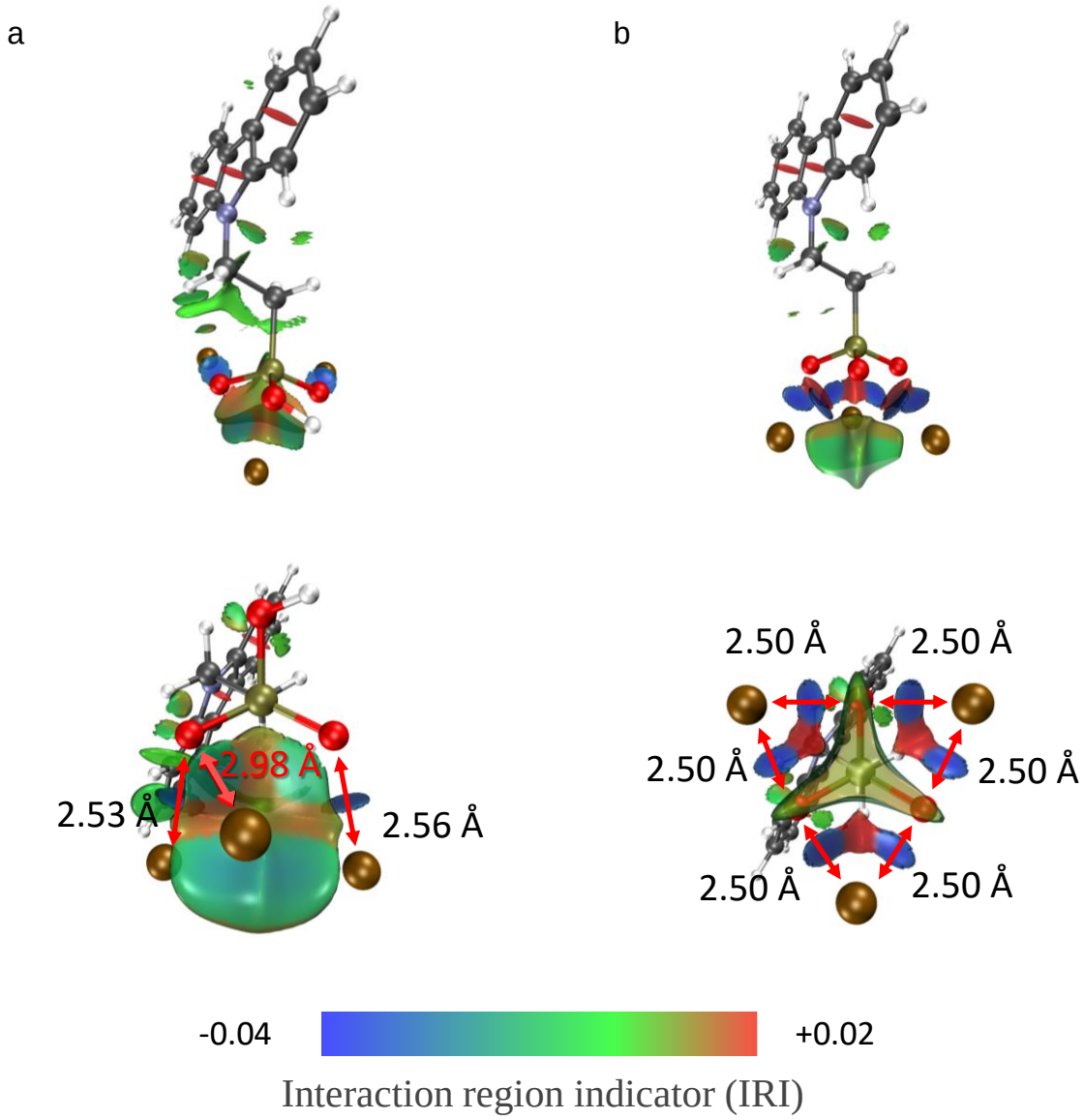

Supplementary Fig. 6. Comparative DFT simulations illustrating the anchoring strength and bond length between 2PACz and ITO substrates prepared via different deposition methods. (a) Spin-coated 2PACz exhibits relatively weaker interactions with the ITO substrate, as indicated by the longer calculated bond lengths. (b) electrodeposited 2PACz shows stronger anchoring interactions with the ITO surface, evidenced by shorter calculated bond lengths.

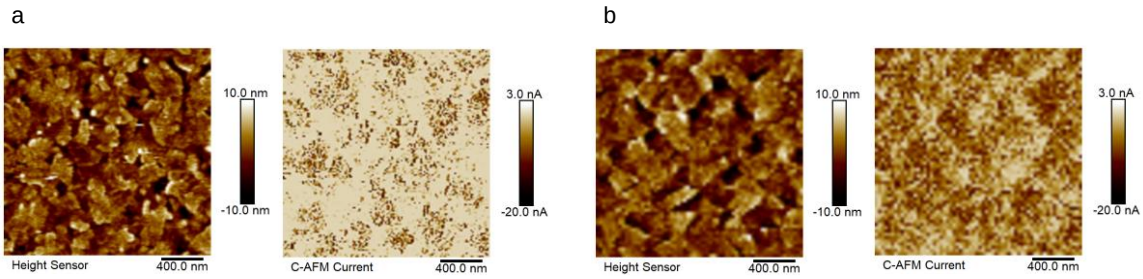

Supplementary Fig. 7. Conductive AFM images demonstrating differences in charge transport pathways and their correlation with the underlying ITO morphology for SAMs fabricated by different methods. (a) Spin-coated 2PACz shows localized, spot-like charge transport channels, which strongly correlate with the ITO substrate topography; notably, enhanced current signals appear primarily at elevated ITO regions, indicating the accumulation of 2PACz in surface recesses during spin-coating. (b) electrodeposited 2PACz displays uniform charge extraction across the entire surface, with significantly reduced morphological dependence, suggesting improved film uniformity and minimized influence from the underlying ITO topography.

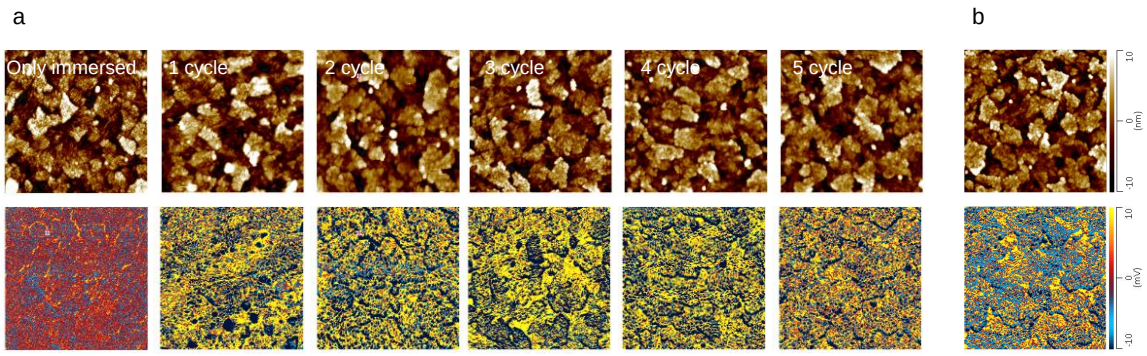

Supplementary Fig. 8. Infrared AFM images of 2PACz SAM layers fabricated by different methods. (a) Electrodeposited 2PACz with varying deposition cycles. When the ITO substrate is simply immersed in the 2PACz solution for 60 s, the infrared signal from 2PACz is negligible. With increasing electrodeposition cycles, the distribution of electrodeposited 2PACz becomes progressively more uniform, and unfilled defective areas diminish gradually. This phenomenon demonstrates the dynamic self-repair capability facilitated by the applied electrochemical potential. (b) spin-coated 2PACz exhibits relatively nonuniform coverage.

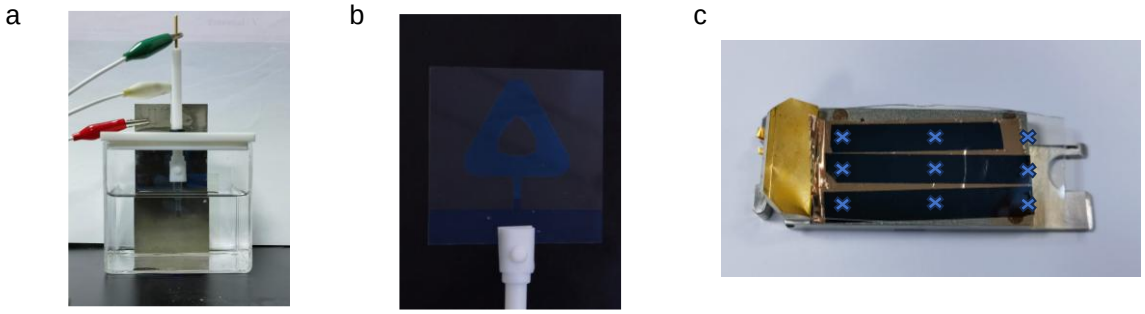

Supplementary Fig. 9. Electrodeposition of SAMs on large-area ITO substrates. (a) Schematic illustration of the electrodeposition setup for SAM fabrication on ITO substrates. (b) photographic image of electrodeposited SAM layer on a 5 × 5 cm ITO substrate. (c) uniformity evaluation of the electrodeposited SAM film demonstrated by X-ray photoelectron spectroscopy (XPS) measurements taken at nine randomly selected spots from the electrodeposited 10 × 10 cm^2 ITO substrate, confirming the consistent film quality and uniform coverage across large-area substrates.

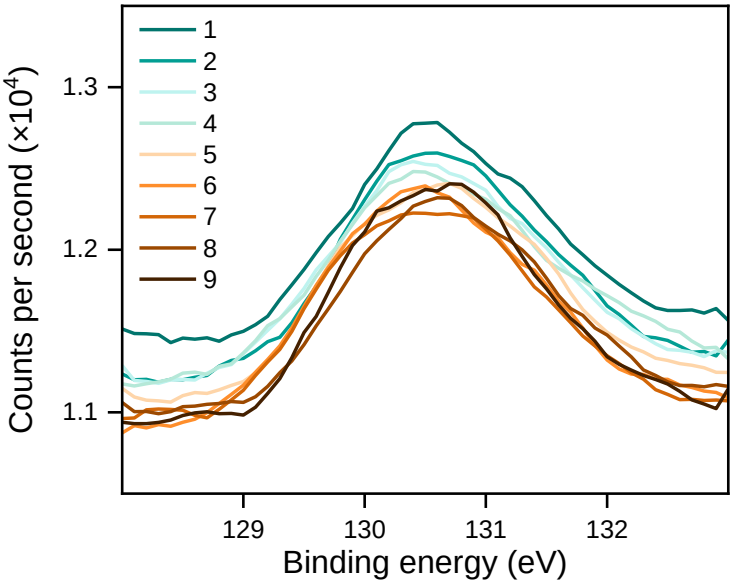

Supplementary Fig. 10. XPS analysis of phosphorus signals measured at nine randomly selected locations across the 10 × 10 cm² electrodeposited ITO/SAM substrate, confirming uniform SAM coverage and demonstrating the scalability and consistency of the electrodeposition method for large-area film preparation.

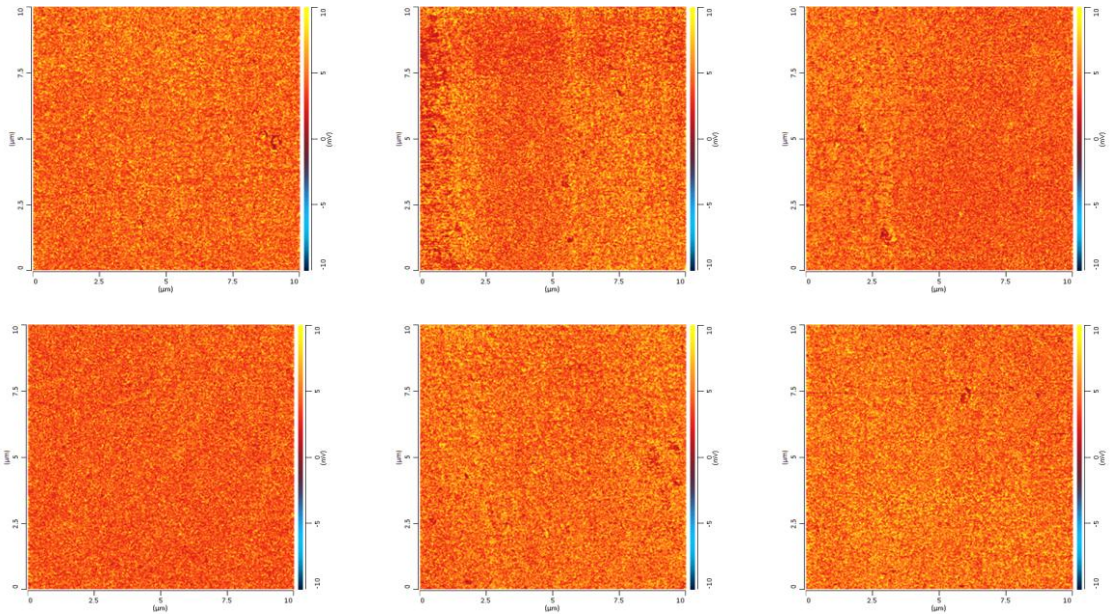

Supplementary Fig. 11. Infrared AFM images taken from six randomly selected locations across the 10 × 10 cm² electrodeposited ITO/SAM substrate, demonstrating highly uniform SAM distribution and confirming the capability of electrodeposition to achieve homogeneous SAM coverage over large-area substrates.

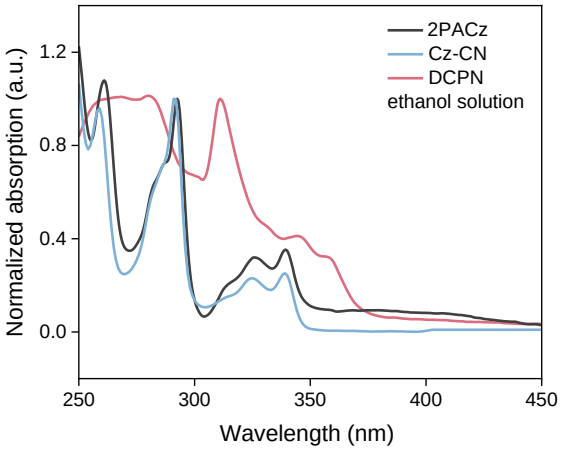

Supplementary Fig. 12. Absorption spectra of 2PACz, Cz-CN, and DCPN.

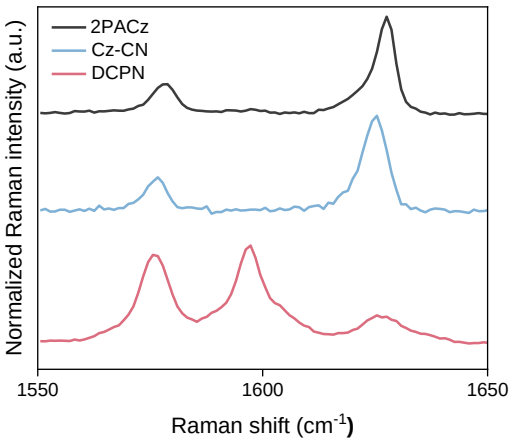

Supplementary Fig. 13. Raman spectra of 2PACz, Cz-CN, and DCPN.

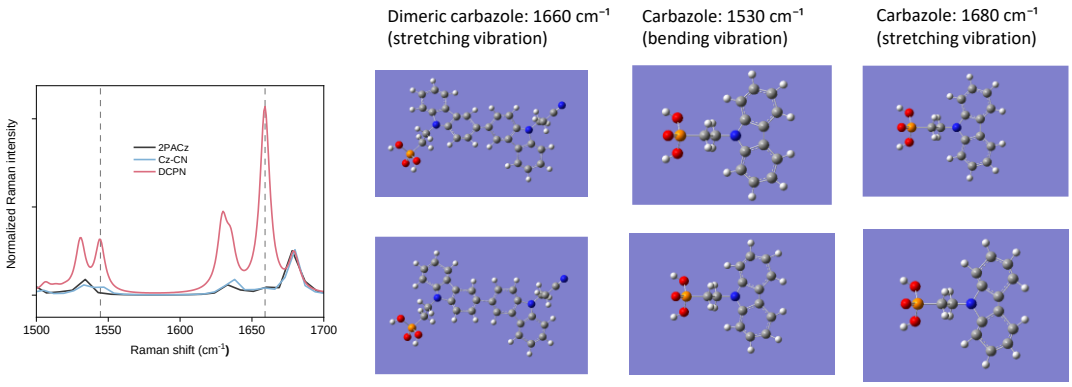

Supplementary Fig. 14. Density function theory(DFT) calculation results of Raman spectra for 2PACz, Cz-CN, and DCPN. The difference in stretching vibrations between dimeric carbazole and monomeric carbazole results in an additional stretching peak for the dimeric carbazole. This observation aligns well with our experimental Raman spectra.

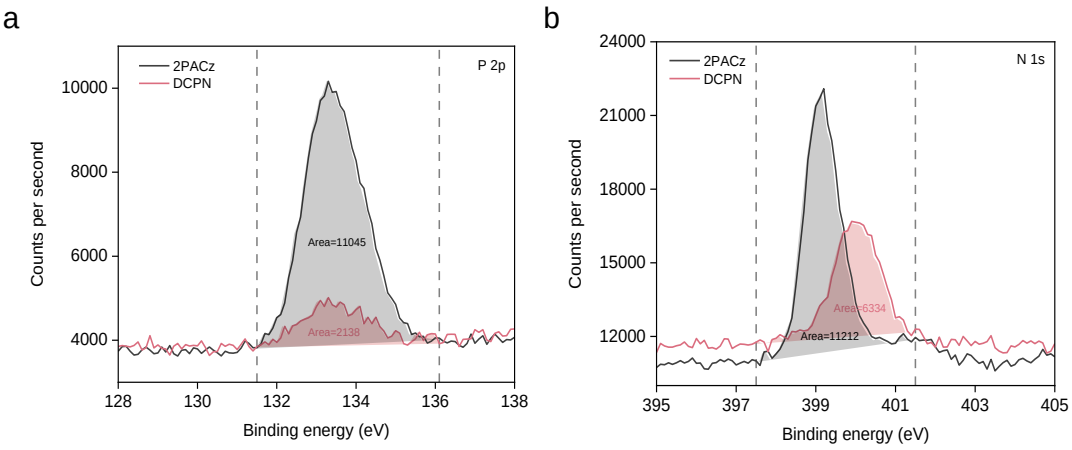

Supplementary Fig. 15. XPS area ratio for 2PACz and DCPN. (a) In P 2p regions (b) In N 1s regions.

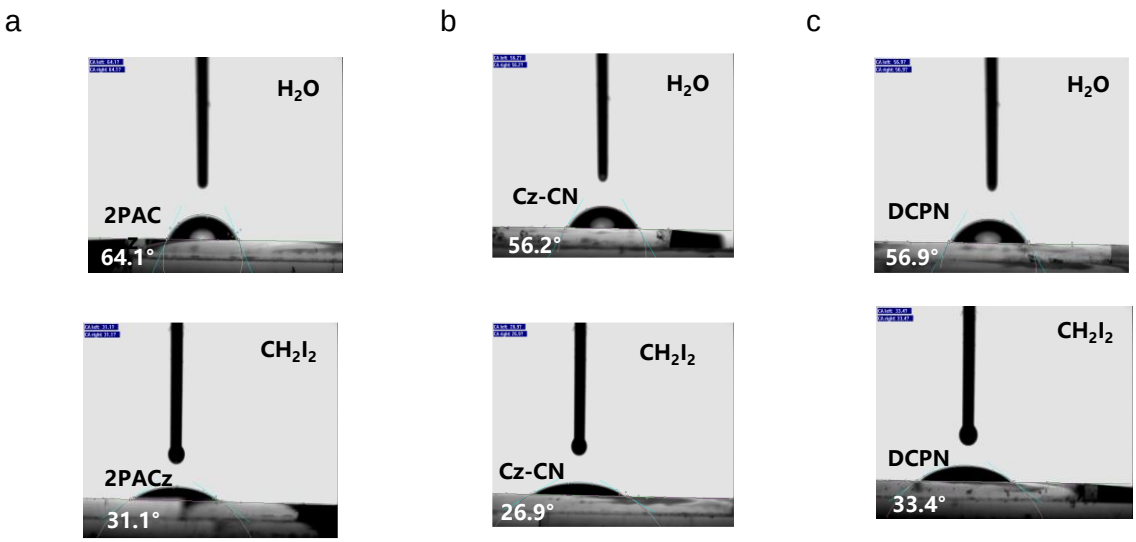

Supplementary Fig. 16. Contact angle measurements of the deposited (a) 2PACz (b) Cz-CN and (c) DCPN film.

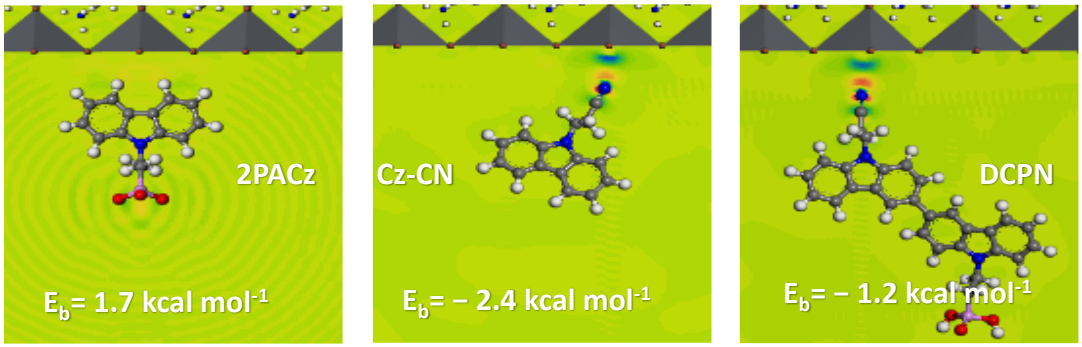

Supplementary Fig. 17. Electron density difference between the perovskite and 2PACz, Cz-CN, DCPN.

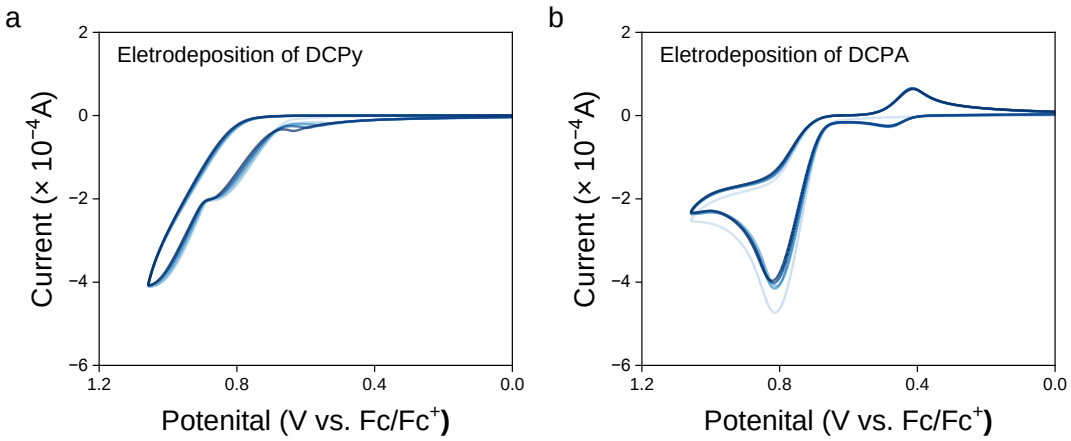

Supplementary Fig. 18. Cyclic voltammogram for the preparation of electrodeposited (a) DCPy (b) DCPA.

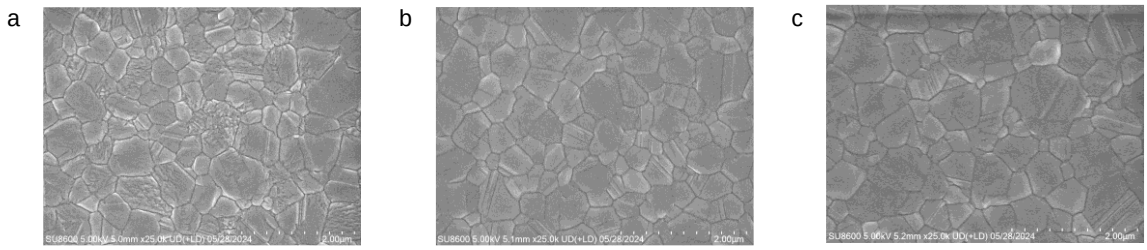

Supplementary Fig. 19. SEM images of the top perovskite interface fabricated on different SAMs.(a) 2PACz (b) Electrodeposited 2PACz (c) Electrodeposited DCPN.

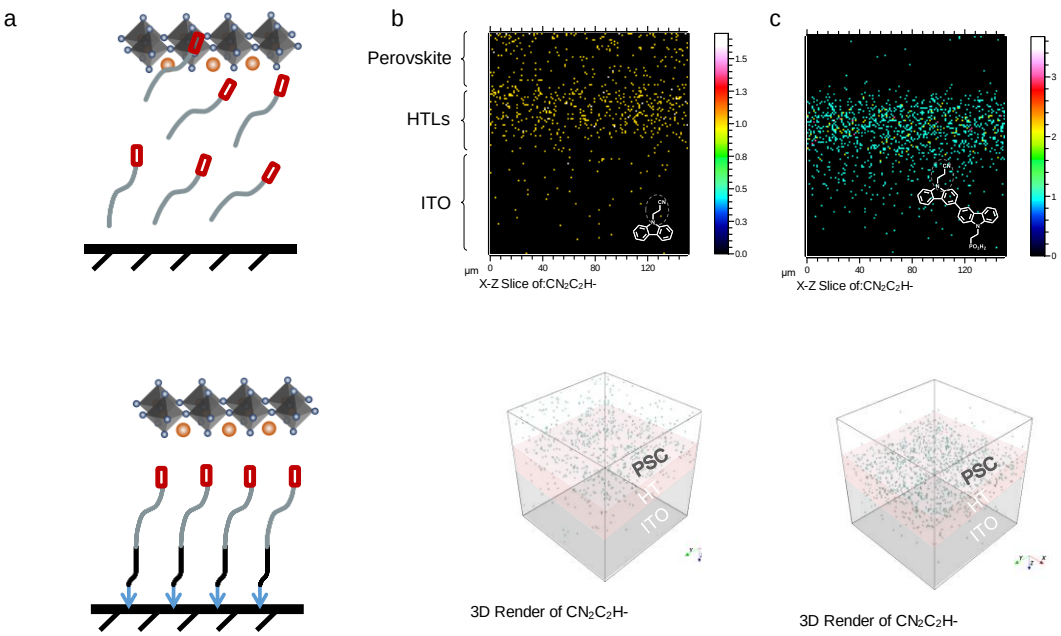

Supplementary Fig. 20. (a) Schematic illustration highlighting the interfacial differences when Cz–CN and electrodeposited DCPN are used as interface layers in perovskite solar cells. Vertical distribution profiles of (b) Cz–CN and (c) DCPN within the perovskite layers, characterized by time-of-flight secondary ion mass spectrometry (TOF-SIMS).

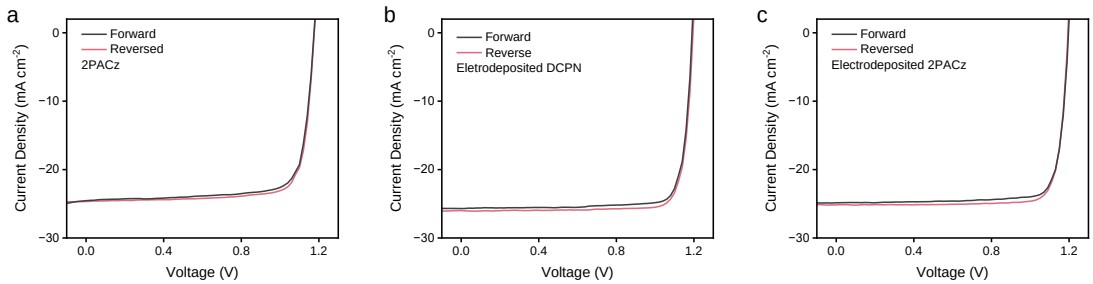

Supplementary Fig. 21. Forward and reverse scan J–V curves of perovskite solar cells based on different SAM layers: (a) 2PACz (b) electrodeposited 2PACz and (c) electrodeposited DCPN.

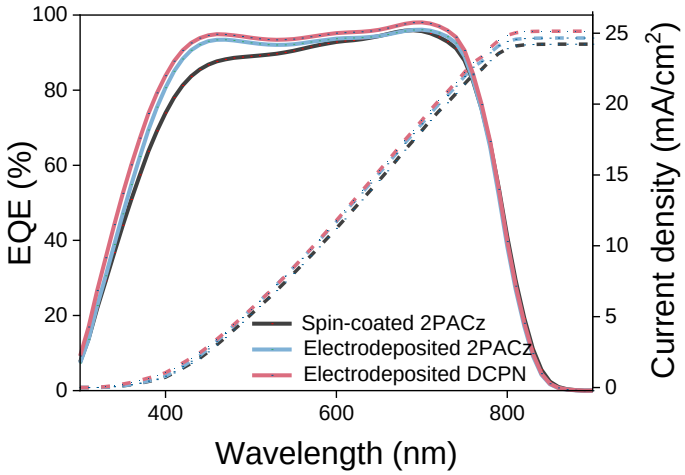

Supplementary Fig. 22. EQE spectra and integrated current densities of perovskite solar cells based on different SAMs.

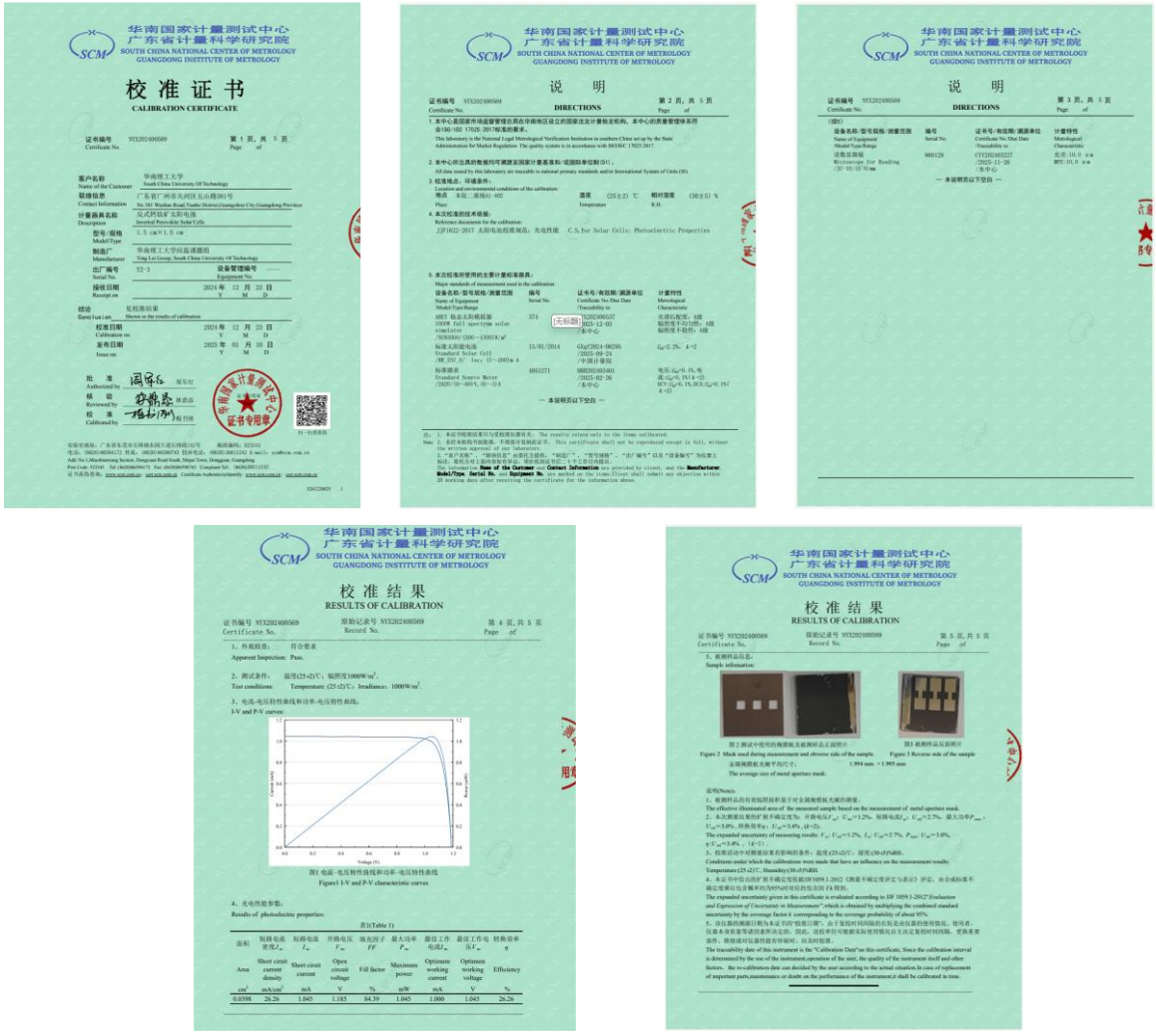

Supplementary Fig. 23. Certified performance of PSCs based on electrodeposited DCPN.

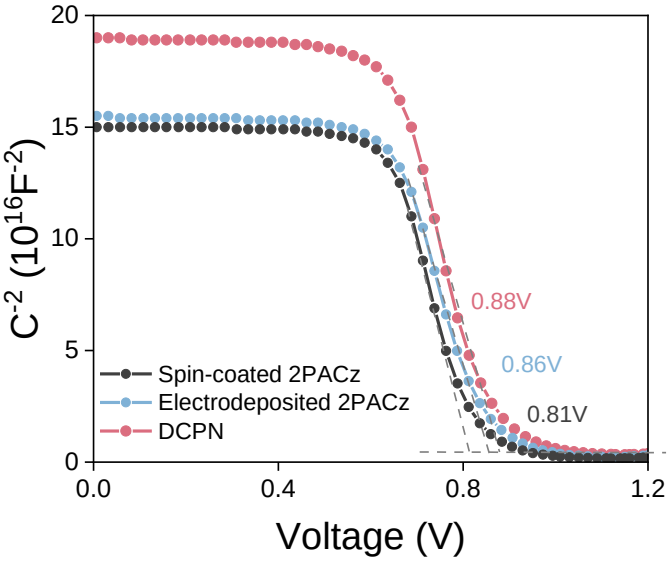

Supplementary Fig. 24. Mott-Schottky plots of C-V characterizations of perovskite solar cells based on different SAMs.

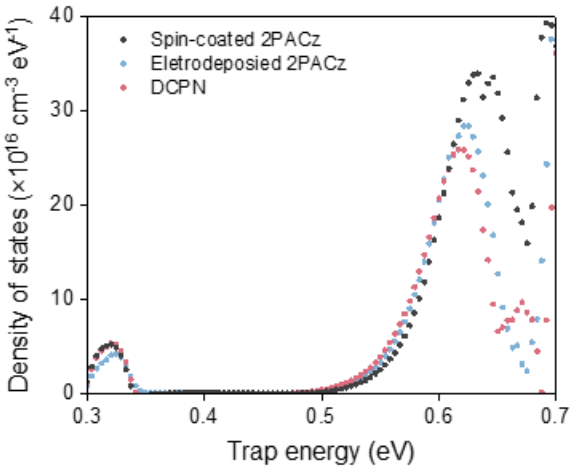

Supplementary Fig. 25. Trap DOS of perovskite solar cells based on different SAMs.

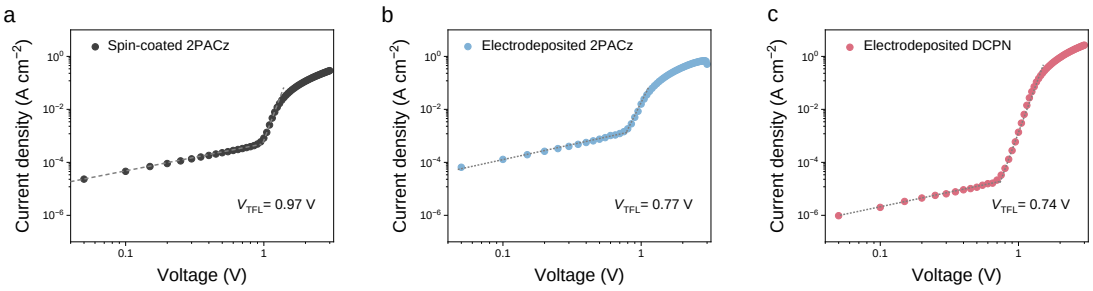

Supplementary Fig. 26. SCLC measurements of the electron-only devices and the hole-only devices based on different SAMs.

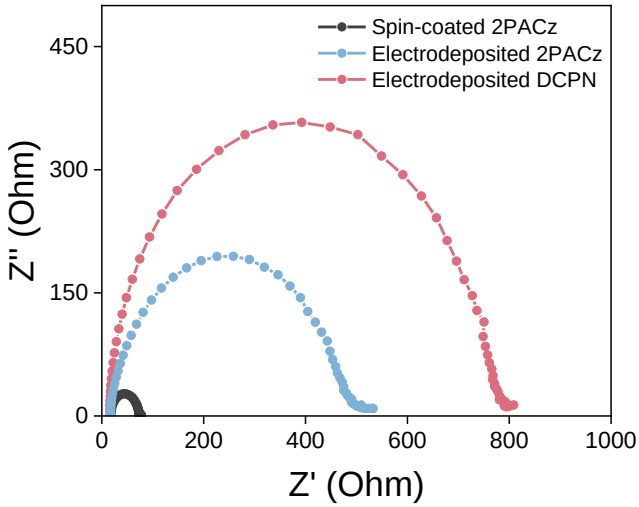

Supplementary Fig. 27. Nyquist plots of EIS spectra of perovskite solar cells based on different SAMs

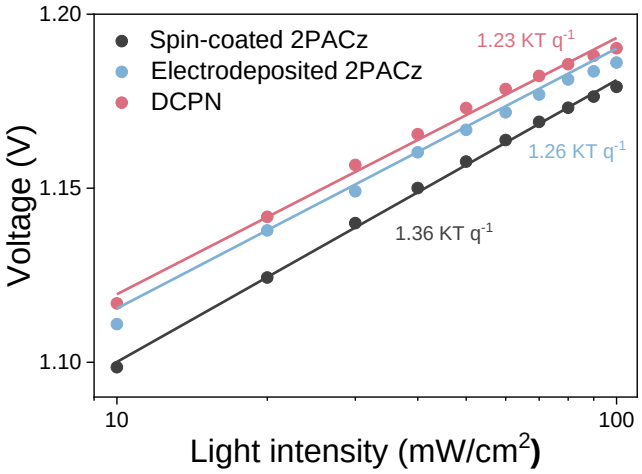

Supplementary Fig. 28. Light intensity dependence of V_{oc} based on different SAMs.

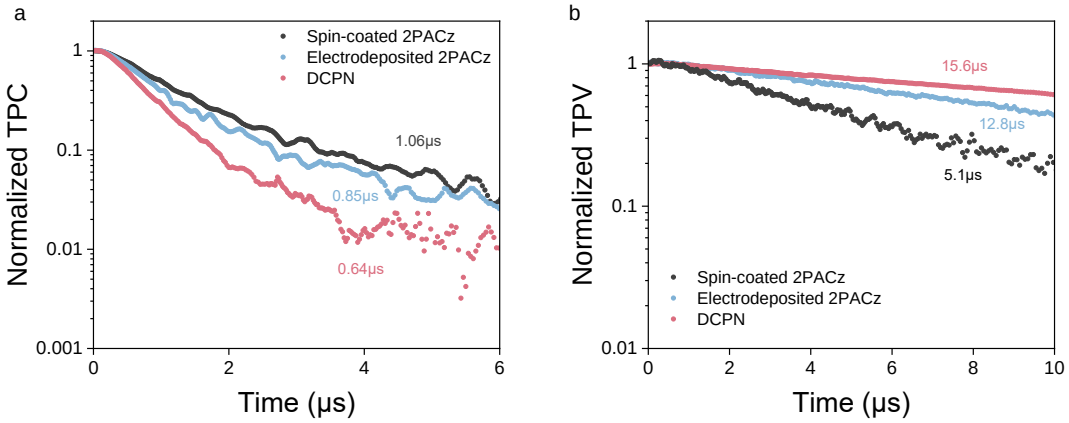

Supplementary Fig. 29. (a)TPC and (b) TPV of perovskite solar cells based on different SAMs.

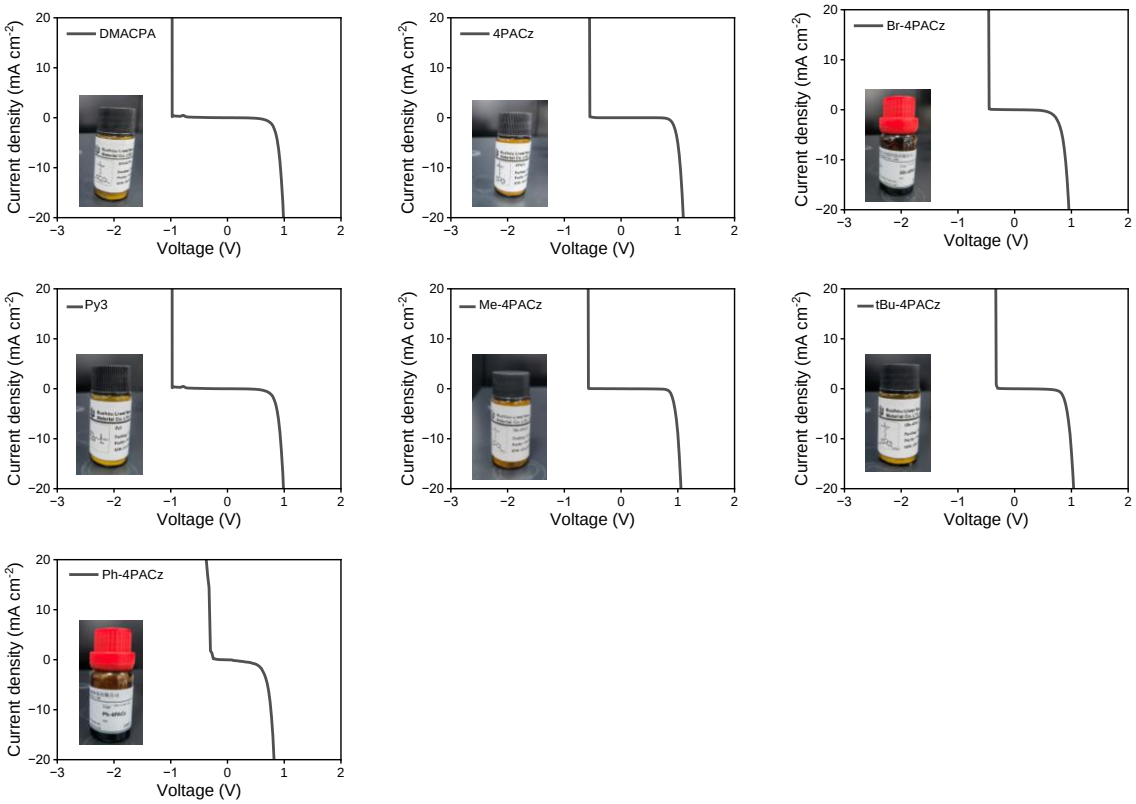

Supplementary Fig. 30. Dark J-V measurements revealing distinct reverse bias behaviors across devices with various SAMs.

Supplementary Table 1. Photovoltaic parameters of solar cells fabricated with different SAMs. Average device characteristics with standard deviation were obtained based on 10 cells for each set.

Device		V_{OC} (V)	J_{SC} (mA/cm2)	**FF(%)**	**PCE(%)**
Spin-coated 2PACz	Best	1.18	24.7	80.8	23.4
	Average	1.17±0.01	24.4±0.4	80.3±0.6	22.9±0.3
Electrodeposited 2PACz	Best	1.19	25.2	84.6	25.0
	Average	1.18±0.01	25.1±0.1	84.0±0.7	25.0±0.3
Electrodeposited DCPN	Best	1.20	26.3	85.9	26.8
	Average	1.19±0.00	26.1±0.2	85.5±0.5	26.3±0.2

Supplementary Table 2. DFT calculated atom coordinates.

For Fig.S6. (A)

Element	X	Y	Z
C	4.318777	3.482981	-0.306103
C	3.065453	3.338926	0.300249
C	2.596021	2.096026	0.703336
C	3.414647	0.992497	0.483278
C	4.681774	1.118725	-0.137741
C	5.130557	2.379085	-0.525844
C	4.27001	-1.088675	0.339719
C	5.231551	-0.215354	-0.227288
C	4.473011	-2.464345	0.387236
C	5.663466	-2.959589	-0.127826
C	6.629059	-2.109703	-0.679748
C	6.419107	-0.739395	-0.73253
N	3.192396	-0.341224	0.790879
C	1.924386	-0.876367	1.228091
C	0.981546	-1.143762	0.049755
P	-0.700635	-1.562504	0.554368
O	-1.57522	-1.81755	-0.660829
O	-0.53686	-2.942446	1.369811
O	-1.193658	-0.490067	1.506092
H	4.655505	4.46648	-0.605807
In	-1.581759	1.930207	0.751103
In	-2.275023	-0.004998	-2.284345
In	-3.942832	-0.672761	0.756052

For Fig.S6. (B)

Element	X	Y	Z
C	6.010107	3.030551	-0.329568
C	4.704784	3.413028	0.001097
C	3.72025	2.471187	0.268342
C	4.075711	1.127493	0.199581
C	5.389555	0.722478	-0.144216
C	6.357737	1.689508	-0.404282
C	4.075363	-1.127458	0.199822
C	5.389333	-0.722932	-0.144052
C	3.719473	-2.471021	0.268926
C	4.703707	-3.413239	0.001902
C	6.009147	-3.031246	-0.328867
C	6.357208	-1.690332	-0.40389
N	3.302328	0.000158	0.42811
C	1.879505	0.000337	0.66824
C	1.066308	-0.000525	-0.630897
P	-0.705114	-0.00032	-0.316061
O	-1.498389	-0.000988	-1.642269
O	-1.088556	-1.258497	0.502775
O	-1.088222	1.258894	0.501406
H	6.752489	3.791128	-0.531668
H	4.455015	4.465078	0.047871
H	2.713467	2.779347	0.516804
H	7.367462	1.398555	-0.665057
H	2.712598	-2.778793	0.517507
H	4.453615	-4.4652	0.048935
H	6.751285	-3.792106	-0.530801
H	7.367026	-1.399766	-0.664734
H	1.627118	-0.874869	1.266311
H	1.627161	0.876371	1.265086
H	1.303332	0.880765	-1.22967
H	1.30364	-0.882389	-1.228693
In	-3.004576	1.891991	-0.982961
In	-3.005001	-1.892365	-0.982207
In	-2.405149	0.000851	2.224436

Supplementary Table 3. Summary of operational stability and reverse-bias breakdown tolerance for PSCs employing different SAMs.

SAMs	Stability after 1000h (%)	Reverse breakdown Voltage (V)	Ref.
MeO-4PACz	79	-0.7	64,65
Ph-4PACz	86	-0.38	66
DMACPA	95	-1.0	67
4PACz	53	-0.56	68
Br-4PACz	93	-0.47	69
Py3	97	-0.99	70
Me-4PACz	80	-0.6	71
tBu-4PACz	90	-0.34	72
2PACz	71	-0.51	-
Electrodeposited 2PACz	98	-1.7	-
Electrodeposited DCPN	99	-2.5	-

References and Notes

49. Li, X. *et al.* Iodine-trapping strategy for light-heat stable inverted perovskite solar cells under ISOS protocols. *Energy Environ. Sci.* **16**, 6071–6077 (2023).
50. Li, L. *et al*. Buried-interface engineering enables efficient and 1960-hour ISOS-L-2I stable inverted perovskite solar cells. *Adv. Mater*. **36**, e2303869 (2024).
51. Peng, W. *et al*. Reducing nonradiative recombination in perovskite solar cells with a porous insulator contact. *Science* **379**, 683–690 (2023).
52. Zhao, Y. *et al*. Inactive $(PbI_2)_2RbCl$ stabilizes perovskite films for efficient solar cells. *Science* **377**, 531–534 (2022).
53. Wu, T. *et al*. Elimination of light-induced degradation at the nickel oxide–perovskite heterojunction by aprotic sulfonium layers towards long-term operationally stable inverted perovskite solar cells. *Energy Environ. Sci*. **15**, 4612–4624 (2022).
54. Peña-Camargo, F. *et al.* Halide segregation versus interfacial recombination in bromide-rich wide-gap perovskite solar cells. *ACS Energy Lett.* **5**, 2728–2736 (2020).
55. Li, L. *et al.* Flexible all-perovskite tandem solar cells approaching 25% efficiency with molecule-bridged hole-selective contact. *Nat. Energy* **7**, 708–717 (2022).
56. Ni, Z. *et al*. Resolving spatial and energetic distributions of trap states in metal halide perovskite solar cells. *Science* **367**, 1352–1358 (2020).
57. Ye, S. *et al.* Expanding the low-dimensional interface engineering toolbox for efficient perovskite solar cells. *Nat. Energy* **8**, 284–293 (2023).
58. Li, T. *et al.* Triisocyanate derived interlayer and high-melting-point doping promoter boost operational stability of perovskite solar cells. *Angew. Chem. Int. Ed*. **63**, e202401604 (2024).
59. Lu, T. & Chen, F. Multiwfn: A multifunctional wavefunction analyzer. *J. Comput. Chem.* **33**, 580–592 (2012).
60. Liu, Z., Lu, T. & Chen, Q. Intermolecular interaction characteristics of the all-carboatomic ring, cyclo[18]carbon: Focusing on molecular adsorption and stacking. *Carbon* **165**, 461–470 (2020).
61. Luo, L. *et al*. Stabilization of 3D/2D perovskite heterostructures via inhibition of ion diffusion by cross-linked polymers for solar cells with improved performance. *Nat. Energy*

8, 294–303 (2023).

62. Liu, C. *et al.* Two-dimensional perovskitoids enhance stability in perovskite solar cells. *Nature* **633**, 359–364 (2024)
63. Chen, Y. *et al*. Strain engineering and epitaxial stabilization of halide perovskites. *Nature* **577**, 209–215 (2020).
64. Jiang, F. et al. Improved reverse bias stability in p–i–n perovskite solar cells with optimized hole transport materials and less reactive electrodes. Nat. Energy **9**, 1275–1284 (2024).
65. Liu, M. *et al.* Defect-passivating and stable benzothiophene-based self-assembled monolayer for high-performance inverted perovskite solar cells. *Adv. Energy Mater.* **14**, 2303742 (2024).
66. Sun, A. *et al.* High open-circuit voltage (1.197 V) in large-area (1 cm^2) inverted perovskite solar cells via interface planarization and a highly polar self-assembled monolayer. *Adv. Energy Mater.* **14**, 2303941 (2024).
67. Tan, Q. et al. Inverted perovskite solar cells using dimethylacridine-based dopants. Nature 620, 545–551 (2023).
68. Huang, Y. *et al.* Asymmetric modification of carbazole-based self-assembled monolayers by a hybrid strategy for inverted perovskite solar cells. *Angew. Chem. Int. Ed.* **64**, e202416188 (2025).
69. Peng, W. et al. A versatile energy-level-tunable hole-transport layer for multi-composition inverted perovskite solar cells. Energy Environ. Sci. **18**, 874–883 (2025).
70. Han, L. Beyond the arylamine convention. Sci. China Mater. **68**, 685–686 (2025).
71. Qu, G. et al. Conjugated linker-boosted self-assembled monolayer molecule for inverted perovskite solar cells. Joule **8**, 2123–2134 (2024).
72. Su, Z. *et al.* Stereo-hindrance-induced conformal self-assembled monolayer for high-efficiency inverted perovskite solar cells. *Small* **20**, 2407387 (2024).